Mechanical Systems and Signal Processing 155 (2021) 107603

Contents lists available at ScienceDirect

Mechanical Systems and Signal Processing

journal homepage: www.elsevier.com/locate/ymssp

A 3-DOF piezoelectric driven nanopositioner: Design, control and experiment

Peng-Zhi Li [a,b,*], De-Fu Zhang [c], Barry Lennox [a], Farshad Arvin [a,*]

[a] *Department of Electrical and Electronic Engineering, The University of Manchester, Manchester M13 9PL, UK*
[b] *School of Computing and Engineering, The University of Gloucestershire, The Park, Cheltenham GL50 2RH, UK*
[c] *Changchun Institute of Optics, Fine Mechanics and Physics, Chinese Academy of Sciences, Changchun 130033, China*

ARTICLE INFO

Article history:
Received 21 September 2020
Received in revised form 5 December 2020
Accepted 29 December 2020
Available online 22 January 2021

Keywords:
Nanopositioner
Walking piezoelectric actuator
Sliding mode control
Flexure
Coupling displacement

ABSTRACT

In this paper, a novel 3-degree-of-freedom (DOF) nanopositioner was investigated in order to position objects with nanometer scale accuracy. Nanopositioners are used in a variety of real-world applications, e.g. biomedical technology and nanoassembly. In this work, a nanopositioner was firstly designed with the flexure diaphragm guider, capacitive sensors and walking piezoelectric actuators. The specifically designed monolithic flexure diaphragm guider was able to significantly restrict motions in the other unwanted directions. The walking piezoelectric actuator can enable the developed nanopositioner to have nanometer scale positioning accuracy and a large travel range. Then a closed-loop sliding mode control strategy was developed to overcome the effect of the actuator's speed nonlinearity and its stability was analysed based on Lyapunov theory. Finally, experiments focused on coupling displacement and point-to-point movement were conducted. The observed results revealed that the ratio of coupling displacement to Z displacement was less than 0.1%, which means that the coupling displacement was less than 120 nm during the Z direction travel range of the nanopositioner from −80 μm to 80 μm. Moreover, the positioning accuracy in the Z direction of point-to-point movement was within 10 nm and the dynamic response settled within 0.2 s. Therefore, the experimental results showed that the novel piezoelectric driven nanopositioner has excellent performance in terms of coupling displacement and nanometer scale accuracy for point-to-point movement.

1. Introduction

As a unit of length in the metric system, the nanometre is equal to one billionth of a meter and is usually used to describe the dimension of an atom. In recent decades, nanorobotics has been widely researched for applications in nanoassembly, biomedical technology and nanoelectromechanical systems, which includes either the robotic manipulation of objects from micrometer to nanometer scale or the design and manufacturing of the robots with dimensions in this range [1–4]. A nanorobot is usually capable of positioning objects of micrometer or nanometer scale. A nanopositioner can position an object with the nanometer scale accuracy although neither itself nor the object that it typically manipulates is in the micrometer to nanometer scale.

---

* Corresponding authors.
E-mail addresses: pli2@glos.ac.uk (P.-Z. Li), farshad.arvin@manchester.ac.uk (F. Arvin).

https://doi.org/10.1016/j.ymssp.2020.107603
0888-3270/

Nanopositioners are usually driven by a voice coil motor or smart material based actuator, e.g. piezoelectric or piezoresistive material, shape memory alloy or polymer, magnetostrictive material or magneto/electrorheological fluid based actuator. Among these actuators, the piezoelectric actuator [5] is widely adopted due to its nanometer scale movement resolution [6–12]. Also, the guiding mechanism of the nanopositioner is often different from the traditional bearing or rolling guide. As an example, a high precision mechanism with a position repeatability of micrometer scale was developed in [13]. The mechanism utilised in this work used flexure bearings and it was actuated by a voice coil motor. In another study [14], a 3-degree-of-freedom (DOF) parallel micro/nano-positioning stage was proposed that was based on a guiding flexure mechanism being driven by three voice coil motors. The stage had a low crosstalk of 1.7% among the three working axes. A 3-DOF micro-stage based on the tripod parallel configuration was developed in [15]. This micro-stage utilized the stacked piezoelectric actuator and flexure hinge mechanism as the actuation unit. The experimental positioning accuracy of the micro-stage was 25 nm. Another study [16] proposed a monolithic 3-DOF adjusting mechanism based on a 6-prismatic-spherical-spherical parallel flexure mechanism and piezoelectric actuator. The axial stroke of the adjusting mechanism was 74.4 μm with an accuracy of within 40 nm. However, the drawback of the studies above was that the coupling displacement was either ignored or significant. A 2-DOF orientation stage driven by 4 stacked piezoelectric actuators for space antenna pointing was presented in [17], in which the rhombic amplifying mechanism and 2D flexure hinge were used to enlarge the workspace and decouple the coupling motion between axes. The proposed stage can achieve approximately ± 1.2 mrad tilt range, as well as the fundamental frequency of 472 Hz. In [18], an XY millimeter-range monolithic flexure mechanism driven by 4 stacked piezoelectric actuators was developed. The hybrid rhombus-lever multistage amplifying mechanism was used, the maximum stroke range of this XY stage was 1.21 mm, and the fundamental frequency was 128 Hz. However, the drawback of these 2 studies was to use 4 stacked piezoelectric actuators for only 2-DOF motions.

In relation to the control strategy [19], advanced control algorithms such as model predictive control [20–22] and sliding mode control [23] have shown some performance advantages over conventional proportional-integral-derivative control in terms of robustness, low sensitivity to parameter uncertainty and external disturbance. A sequential control scheme composed of a proportional-integral controller for the coarse dynamics and a gain-scheduled H_∞ controller for the fine dynamics was proposed for a 3-DOF XY$\theta_Z$micro positioning platform in [24]. Another study [25] developed a real-time hybrid control strategy that employed an inverse hysteresis model-based, feedforward controller that was combined with a proportional-integral-derivative feedback controller to achieve a sub-micron accuracy for the 3-DOF XYZ micropositioning system. A combined feedforward/feedback control methodology was proposed for a 3-DOF XY$\theta_Z$planar flexure-based micro/nano-positioning mechanism in [26]. In another study [27], a robust adaptive control methodology was presented to enhance the tracking performance of a monolithic 3-DOF XYZ micro/nano manipulator. However, their proposed control strategies were mainly developed to deal with the hysteresis nonlinearity of the stacked piezoelectric actuators.

In the previous works discussed above, there were typically limitations in either travel range or positioning accuracy. There was also unwanted coupling displacement which was ignored, despite being significant in some studies. In order to investigate a stage with excellent performance in terms of coupling displacement and nanometer scale accuracy, in this paper, a novel 3-DOF nanopositioner was developed based on a specifically designed flexure diaphragm guider and walking piezoelectric actuators. One of the potential applications of the nanopositioner is in the lithographic objective lens. The other applications are in biomedical devices, robotics and even to structural dynamics systems. Also, implementation of nanorobotics in real-time structural modal control using eigenvalue perturbation and Kalman Filter methods is another application of our work. The main contributions of this paper are: (1) the monolithic flexure diaphragm guider is able to significantly restrict other unwanted motions, thus making the coupling displacement less than 120 nm during the travel range of the nanopositioner, (2) the walking piezoelectric actuator (WPA) can provide nanometer scale movement resolution during its millimeter scale travel range, which enables the developed nanopositioner to have nanometer scale positioning accuracy and a large travel range, and (3) the closed-loop sliding mode control strategy is developed with displacement feedback provided by the capacitive sensor, which guarantees nanometer scale positioning accuracy and the fast dynamic response of the nanopositioner whilst overcoming the effect of the speed nonlinearity of the WPA.

The remainder of this paper is organised as follows: in Section 2 the nanopositioner design is presented, Section 3 develops the closed-loop control strategy, Section 4 includes the experimental results, Section 5 presents further discussions, and in Section 6 the conclusion of the paper is provided.

2. Design

This section focuses on three main objectives of the design properties, which are the mechanism, capacitive sensing, and walking piezoelectric actuation.

2.1. Mechanism

As shown in Fig. 1(a), in addition to the walking piezoelectric actuator and capacitive sensor, the mechanism of the developed 3-DOF nanopositioner consists of 5 major parts: lever, spring, fixed base, movable part and flexure diaphragm guider. Other parts, such as fasteners are not included in this figure for brevity. The lever transmits the motion of the WPA to the movable part through a certain ratio and a changing direction in motion. The lever changes the transmission direction of

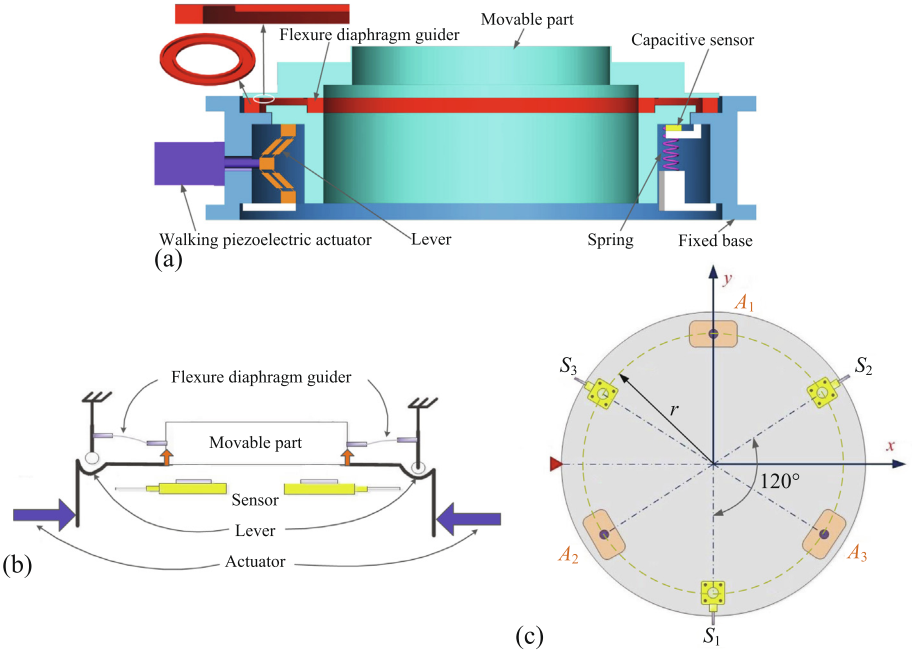

Fig. 1. (a) The mechanism diagram, (b) working principle, and (c) layouts of actuators (A_{1-3}) and sensors (S_{1-3}). r is the radius of layout circumference of sensors.

motion of the WPA. Direction of the output motion of the lever is vertical to the motion of the WPA. The lever is made of a flexure hinge based, bridge-type amplifying mechanism. The spring is to balance the gravity of the movable part so that the force generated by the WPA can be used for improving the fast dynamic response of the movable part. There are in total 6 springs inside the mechanism. The fixed base serves as a stationary outer housing and frame. The movable part is able to move with 3-DOF and holds the external payload. The flexure diaphragm guider plays an important role in guiding the motion of the movable part in the designated directions. Compared with the traditional flexure hinge based guider, the flexure diaphragm guider is more capable of restricting motion in unwanted directions with reduced concentrations of stress.

The working principle of the mechanism is illustrated in Fig. 1(b). The WPA generates linear motion. The lever changes the direction of the motion and transmits the motion to the movable part. The movable part then moves in the specified directions through the flexure diaphragm guider. Meanwhile, the sensor continuously measures the displacement of the movable part at a particular location.

The layouts of the actuators and sensors in the mechanism are indicated in Fig. 1(c). There are 3 WPAs and 3 capacitive sensors uniformly installed along the circumference of the fixed base. The parallel mechanism is simultaneously driven by 3 WPAs A_1, A_2 and A_3, and is essentially a tripod in structure. The capacitive sensors (S_1, S_2 and S_3) measure the linear displacement of the movable part at 3 different locations. The pose Z, θ_x and $\theta_y$of the movable part along $z$axis, around $x$and $y$axes rotation can be computed using the following equation:

$$\begin{aligned} Z &= \frac{S_1+S_2+S_3}{3}, \\ \theta_x &= \frac{S_2+S_3-2S_1}{3r}, \\ \theta_y &= \frac{S_3-S_2}{\sqrt{3}\,r}, \end{aligned} \tag{1}$$

where r is the distance of the sensors from the center of the moving part. Hence, this equation can be rewritten as

$$\begin{bmatrix} Z \\ \theta_x \\ \theta_y \end{bmatrix} = \begin{bmatrix} \frac{1}{3} & \frac{1}{3} & \frac{1}{3} \\ -\frac{2}{3r} & \frac{1}{3r} & \frac{1}{3r} \\ 0 & -\frac{1}{\sqrt{3}r} & \frac{1}{\sqrt{3}r} \end{bmatrix} \begin{bmatrix} S_1 \\ S_2 \\ S_3 \end{bmatrix} = \mathbf{M}_{\mathrm{S2P}} \cdot \begin{bmatrix} S_1 \\ S_2 \\ S_3 \end{bmatrix}, \tag{2}$$

where the matrix $\mathbf{M}_{\mathrm{S2P}}$ is the transformation relationship from the displacement measurement of the capacitive sensors to the pose of the movable part.

The kinematics relationship of motion transmission from the three piezoelectric actuators to the capacitive sensors can be expressed as

$$\begin{bmatrix} S_1 \\ S_2 \\ S_3 \end{bmatrix} = \begin{bmatrix} \mathbf{J}_{11} & \mathbf{J}_{12} & \mathbf{J}_{13} \\ \mathbf{J}_{21} & \mathbf{J}_{22} & \mathbf{J}_{23} \\ \mathbf{J}_{31} & \mathbf{J}_{32} & \mathbf{J}_{33} \end{bmatrix} \begin{bmatrix} A_1 \\ A_2 \\ A_3 \end{bmatrix} = \mathbf{J} \cdot \begin{bmatrix} A_1 \\ A_2 \\ A_3 \end{bmatrix}, \tag{3}$$

where the matrix $\mathbf{J}$ is the motion transmission relationship from the displacement of piezoelectric actuators to the displacement measurement of the capacitive sensors.

The result of a modal analysis of the mechanism is shown in Fig. 2. The modal analysis was executed in ANSYS software and based on finite element analysis (FEA). The used material of this mechanism was type 431 stainless steel. Regarding the FEA model, the higher order 3-D 20-node solid element SOLID186 was used, which can exhibit quadratic displacement behavior. In addition, the mesh size of the flexure hinges was specially refined for more accurate simulation results. The element type and mesh size used in ANSYS FEA are listed in Table 1. The first order resonant frequency of the mechanism was 173.19 Hz around $y$axis rotation, while the second and third order resonant frequencies were 173.27 Hz around $x$axis rotation and 193.68 Hz along $z$axis, respectively.

2.2. Capacitive sensor

The capacitive sensor [28] is a non-contact and absolute displacement sensor with compact structure and small installation space. Based on the ideal plate capacitor principle, the measured object (conductor or semiconductor) and capacitive sensor can each be regarded as a plate electrode as shown in Fig. 3. When a sinusoidal voltage of a particular frequency is applied to the capacitive sensor, the change in the amplitude of this voltage is proportional to the distance between

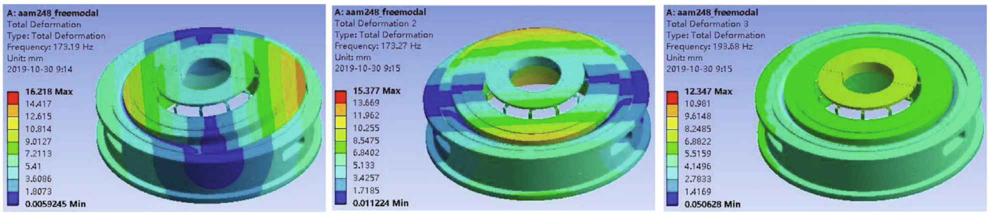

Order 1, 173.19 Hz Order 2, 173.27 Hz Order 3, 193.68 Hz

Fig. 2. The modal analysis of the mechanism.

Table 1
The element type and mesh size which were used in ANSYS FEA.

No.	Model	Element type	Node	Mesh size
1	Lever	SOLID186	3-D 20-node	0.3 mm
2	Flexurediaphragm guider	SOLID186	3-D 20-node	0.3 mm
3	Remaining parts	SOLID186	3-D 20-node	3 mm

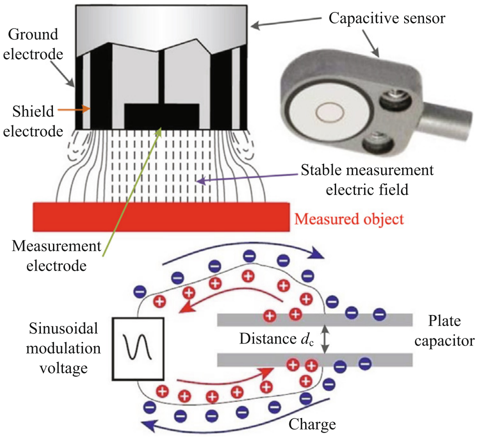

Fig. 3. The diagram of capacitive sensor.

the capacitive sensor and the measured object. The impedance value $X_c$of the plate capacitor formed by the capacitive sensor and the measured object can be described by the following equation:

$$X_c = \frac{d_c}{j\omega_c\varepsilon_c A_c}, \tag{4}$$

where ω_c represents the modulation frequency, ε_c, A_c and d_c represents the dielectric constant (permittivity) of the filling medium, the formed effective area and the distance between the two plates, respectively. When the dielectric constant ε_c, plate area A_c and modulation frequency ω_c are constant, the impedance value $X_c$of the capacitive plate is proportional to the distance d_c between the two plates, hence the displacement can thus be measured by modulating and processing the impedance value.

The high-precision measurement system of the capacitive sensor is generally composed of a capacitance measurement probe, a signal preamplifier and a signal conditioner. The capacitance measurement probe has a ground electrode, a shield electrode and a measurement electrode, which can generate a uniform and stable measurement electric field as described in (4).

The displacement measurement noise of the adopted capacitive sensor when mounted on the developed nanopositioner is shown in Fig. 4. The Peak-to-Valley (PV) value of the measurement noise of a single capacitive sensor was 11 nm.

2.3. Walking Piezoelectric Actuator (WPA)

Compared with the classical stacked piezoelectric actuator, WPA is capable of holding its position when there is no power. Furthermore, the WPA has millimeter-scale travel range whilst maintaining nanometer-scale resolution. As shown in Fig. 5, the adopted WPA is mainly composed of two pairs of piezoelectric legs and a moving rod, and the piezoelectric legs are brought into contact with the moving rod by a certain initial preload [29]. The same driving voltage waveforms are applied to each pair of piezoelectric legs, and the two pairs of piezoelectric legs alternately complete the motion transmission with the moving rod, thereby generating continuous displacement of the moving rod during a walking period. A pair of piezoelectric legs (A, D or B, C) is composed of two piezoelectric legs, and each piezoelectric leg is composed of two piezoelectric stacked actuators. The two stacked actuators of a piezoelectric leg are mechanically fixed together but electrically insulated so that they can be excited with different driving voltages (V_1, V_2or V_3, V_4). When the driving voltages that are applied to the two stacked actuators of a piezoelectric leg are identical at some time instant, then the piezoelectric leg will produce the

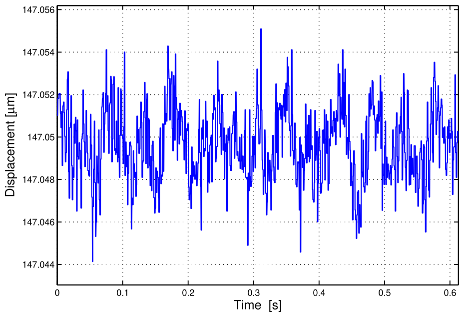

Fig. 4. The displacement measurement noise of capacitive sensor.

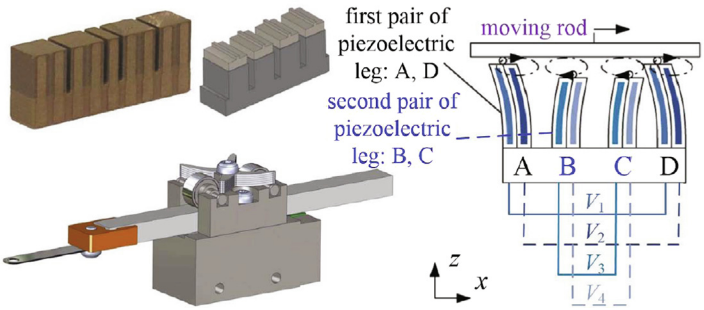

Fig. 5. The working principle of WPA.

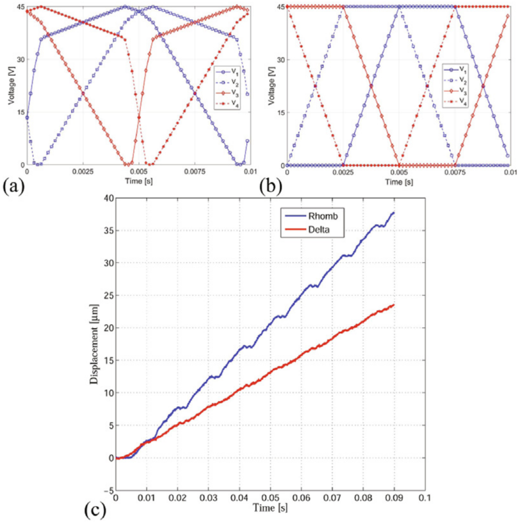

Fig. 6. The driving voltage waveforms (a) Delta type and (b) Rhomb type, and (c) step length of WPA.

corresponding movement only in the z direction. When the driving voltages are different, the piezoelectric leg will be bent and deformed in the $x$direction, and thus the moving rod will move in the x direction.

Different driving voltage waveforms will generate different cyclic trajectories of the piezoelectric legs, thus producing different displacement characteristics of the WPA in the $x$direction. As illustrated in Fig. 6a) and Fig. 6(b), there are two different driving voltage waveforms referred to as Delta and Rhomb types. And as shown in Fig. 6(c), the moving step length of WPA under these two types of voltage waveforms are approximately 3 μm and 4.7 μm, respectively. The movement under Delta type waveform is relatively smoother than that under Rhomb type although the step length is smaller.

In this paper, for the practical application of WPA, the Delta type waveform (shown in Fig. 6a) was chosen to excite the WPA due to its smooth movement. Varying speed was obtained via changing the frequency of the voltage waveform and hence, the input voltage u_a to the power amplifier for driving the WPA is treated as the frequency of the voltage waveform, thus corresponding to the moving speed of WPA. A simplified second order transfer function of WPA [8] from the input voltage u_a to the displacement $x$of the WPA can be expressed as

$$\frac{x(s)}{u_a(s)} = \frac{k_a}{s(\mathrm{T}_a s + 1)} = \frac{k_a}{\mathrm{T}_a s^2 + s}, \tag{5}$$

where s, k_a and T_a are the Laplace variable, the speed gain and inertial constant of WPA, respectively.

3. Control

The utilised closed-loop control strategy of the holistic nanopositioner is shown in Fig. 7. The control algorithm is composed of the inverse of the transformation matrix $\mathbf{M}_{\mathrm{S2P}}$in (2) and the motion transmission matrix $\mathbf{J}$in (3), combined with a sliding mode controller. The displacement feedback is achieved using the capacitive sensor. When the desired pose $P_d = [\mathrm{Z}, \theta_x, \theta_y]^T$ is an input to the closed-loop controller, the inverse matrix $\mathbf{M}_{\mathrm{S2P}}^{-1}$ transforms it to the desired displacement S_d, then the displacement error can be computed with the feedback of the real displacement $S_r = [S_1, S_2, S_3]^T$ measured by the capacitive sensor. The desired movement of the WPA is then computed via the inverse matrix $\mathbf{J}^{-1}$ and subsequently acts as the input to the sliding mode controller. The inverse matrix $\mathbf{J}^{-1}$ is able to compensate for the static coupling effect of the 3 actuator inputs and 3 sensor measurement outputs of the parallel 3-DOF nanopositioner.

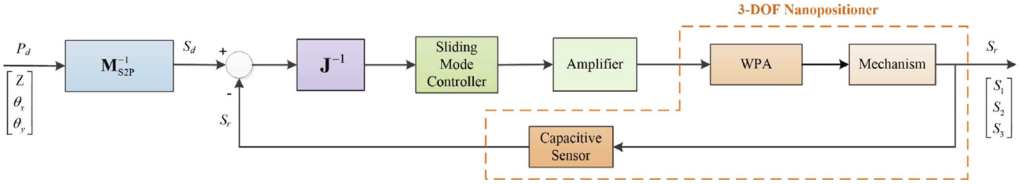

Fig. 7. Block diagram of the controller.

According to (5), the WPA can be described as

$$\ddot{x} = \ddot{x}(t) = -\frac{1}{\mathrm{T}_a}\dot{x}(t) + \frac{k_a}{\mathrm{T}_a}u_a(t) + d(t), \tag{6}$$

where $d = d(t)$ is an external disturbance and unmodelled nonlinearity, $|d| \leqslant \delta$.

The displacement error $e$is defined as

$$e = x_d - x, \tag{7}$$

where x_d is the desired displacement.

The sliding mode function [23,30] is chosen as

$$\mathrm{S} = \mathrm{S}(x,t) = \dot{e} + \lambda e, \tag{8}$$

where λsatisfies the Hurwitz condition, $\lambda > 0$.

Then an exponential reaching law of sliding mode is adopted as

$$\dot{\mathrm{S}} = -\gamma\mathrm{S} - \beta\tanh\left(\frac{\mathrm{S}}{\eta}\right), \gamma > 0, \beta > 0, \eta > 0, \tag{9}$$

where tanh is the hyperbolic tangent function [31] with the following form

$$\tanh\left(\frac{\mathrm{S}}{\eta}\right) = \frac{\mathrm{e}^{\frac{\mathrm{S}}{\eta}} - \mathrm{e}^{-\frac{\mathrm{S}}{\eta}}}{\mathrm{e}^{\frac{\mathrm{S}}{\eta}} + \mathrm{e}^{-\frac{\mathrm{S}}{\eta}}}. \tag{10}$$

Finally, the sliding mode controller is designed as

$$u = \frac{\mathrm{T}_a}{k_a}\left(\gamma\mathrm{S} + \beta\tanh\left(\frac{\mathrm{S}}{\eta}\right)\right) + \frac{\mathrm{T}_a}{k_a}\left(\ddot{x}_d + \frac{1}{\mathrm{T}_a}\dot{x} + \lambda(\dot{x}_d - \dot{x}) + \delta\tanh\left(\frac{\mathrm{S}}{\eta}\right)\right). \tag{11}$$

Regarding the stability of the designed sliding mode controller, 2 lemmas [32,33] are firstly introduced and their detailed proofs are included in Appendix A and B.

Lemma 1. *For every given scalar $\psi \in \mathbb{R}$ and positive scalar η, the following inequality holds:*

$$0 \leqslant |\psi| - \psi\tanh\left(\frac{\psi}{\eta}\right) \leqslant \xi\eta, \xi = 0.2785. \tag{12}$$

Lemma 2. *Suppose $f, \mathrm{V} : [0,\infty) \in \mathbb{R}$, then for any finite constant $\alpha, \dot{\mathrm{V}} \leqslant -\alpha\mathrm{V} + f, \forall t \geqslant t_0 \geqslant 0$ implies that*

$$\mathrm{V}(t) \leqslant \mathrm{e}^{-\alpha(t-t_0)}\mathrm{V}(t_0) + \int_{t_0}^{t}\mathrm{e}^{-\alpha(t-\tau)}f(\tau)d\tau. \tag{13}$$

Based on (7) and (8), the following equation is obtained as

$$\dot{\mathrm{S}} = \ddot{e} + \lambda\dot{e} = (\ddot{x}_d - \ddot{x}) + \lambda(\dot{x}_d - \dot{x}). \tag{14}$$

Substituting (6) into (14), we will have

$$\dot{\mathrm{S}} = (\ddot{x}_d + \frac{1}{\mathrm{T}_a}\dot{x} - \frac{k_a}{\mathrm{T}_a}u_a - d) + \lambda(\dot{x}_d - \dot{x}). \tag{15}$$

Replacing $u_a$in (15) with the control law $u$in (11), then the following equation holds:

$$\begin{aligned}\dot{\mathrm{S}} &= -\gamma\mathrm{S} - \beta\tanh\left(\tfrac{\mathrm{S}}{\eta}\right) - \delta\tanh\left(\tfrac{\mathrm{S}}{\eta}\right) - d \\ &= -\gamma\mathrm{S} - (\beta+\delta)\tanh\left(\tfrac{\mathrm{S}}{\eta}\right) - d \\ &= -\gamma\mathrm{S} - \tilde{\delta}\tanh\left(\tfrac{\mathrm{S}}{\eta}\right) - d,\end{aligned} \tag{16}$$

where $\tilde{\delta} = \beta + \delta$.

The Lyapunov function is chosen as

$$\mathrm{V} = \frac{1}{2}\mathrm{S}^2, \tag{17}$$

then

$$\dot{V} = S\dot{S} = S\left(-\gamma S - \delta \tanh\left(\frac{S}{\eta}\right) - d\right) = -\gamma S^2 + \left(-\tilde{\delta} S \tanh\left(\frac{S}{\eta}\right) - Sd\right). \tag{18}$$

Based on Lemma 1, we have

$$\tilde{\delta}|S| - \tilde{\delta} S \tanh\left(\frac{S}{\eta}\right) \leqslant \tilde{\delta}\xi\eta, \tag{19}$$

then

$$-\tilde{\delta} S \tanh\left(\frac{S}{\eta}\right) \leqslant -\tilde{\delta}|S| + \tilde{\delta}\xi\eta. \tag{20}$$

Substituting (20) into (18), we have

$$\begin{aligned} \dot{V} &\leqslant -\gamma S^2 + \left(-\tilde{\delta}|S| + \tilde{\delta}\xi\eta - Sd\right) \\ &= -\gamma S^2 + \left(\tilde{\delta}\xi\eta + \left(-\tilde{\delta}|S| - Sd\right)\right) \\ &\leqslant -\gamma S^2 + \tilde{\delta}\xi\eta \\ &= -2\gamma V + \tilde{\delta}\xi\eta, \end{aligned} \tag{21}$$

then $\dot{V} \leqslant -2\gamma V + \tilde{\delta}\xi\eta$.

According to Lemma 2, we can get

$$\begin{aligned} V(t) &\leqslant e^{-2\gamma(t-t_0)}V(t_0) + \int_{t_0}^{t} e^{-2\gamma(t-\tau)}\tilde{\delta}\xi\eta d\tau \\ &= e^{-2\gamma(t-t_0)}V(t_0) + \frac{\tilde{\delta}\xi\eta}{2\gamma}\left(1 - e^{-2\gamma(t-t_0)}\right), \end{aligned} \tag{22}$$

then

$$\lim_{t\to\infty} V(t) \leqslant \frac{\tilde{\delta}\xi\eta}{2\gamma} = \frac{(\beta+\delta)\xi\eta}{2\gamma}. \tag{23}$$

Hence, according to the inequality in (23), the designed sliding mode controller for the nanopositioner is asymptotically stable. Moreover, substituting (17) and (8) into (23), we can get the solution as

$$\lim_{t\to\infty} |e(t)| \leqslant \frac{1}{\lambda}\sqrt{\frac{(\beta+\delta)\xi\eta}{\gamma}} \approx \frac{0.5278}{\lambda}\sqrt{\frac{(\beta+\delta)\eta}{\gamma}}, \tag{24}$$

which shows the convergence value of displacement error is bounded by the parameters $\lambda, \gamma, \beta, \delta$ and η.

For the sliding mode control strategy, λ is firstly chosen to construct a sliding surface in (8) and the larger the value is, the faster will be the convergence speed of the sliding phase to equilibrium. Then γ and β are designed for the exponential reaching law of the sliding mode. A larger value for γ typically means faster convergence speed of the reaching phase to sliding surface. The smaller the value for β is, generally, the less chattering of the control output $u$in (11) there will be. Moreover, the tanhfunction is adopted to reduce the chattering, and a smaller ηvalue means that the tanhfunction can better approximate the discontinuous signfunction but cause more chattering. Finally, δ is used to overcome the effect of external disturbance and parametric uncertainty, with a larger value in more robustness but more severe chattering.

4. Experiment

4.1. Experimental platform

As illustrated in Fig. 8, the experimental platform for the developed 3-DOF nanopositioner consists of: 1) WPA, 2) mechanism with built-in sensors, 3) sensor signal conditioner and 4) digital signal processor (DSP)-based controller. There are 3 WPAs installed outside of the mechanism and 3 capacitive sensors mounted inside of the mechanism. The sensor signal conditioner converts the displacement value measured by the capacitive sensor to the proportional electronic signal. The corresponding displacement signal from the sensor signal conditioner is sent to the DSP-based controller. The controller is composed of a TI (Texas Instruments) OMAP L138 DSP and 3 power amplifiers. The developed closed-loop control algorithm of the holistic nanopositioner was implemented using the DSP micro-controller. Based on the controller output signal, the power amplifier excited the WPA with the driving voltage of the corresponding frequency.

The servo period of the proposed closed-loop control algorithm is 0.2 ms. When the units of displacement and angle are μm and μrad, respectively, the matrix $\mathbf{M}_{S2P}$ and $\mathbf{J}$ are

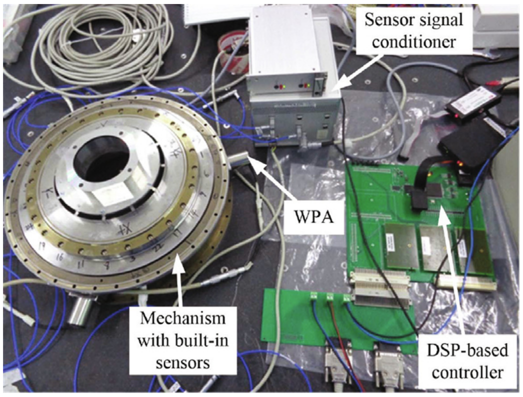

Fig. 8. The experimental platform for the developed 3-DOF nanopositioner.

$$\mathbf{M}_{\mathrm{S2P}} = \begin{bmatrix} 0.333333 & 0.333333 & 0.333333 \\ -3.836930 & 1.918465 & 1.918465 \\ 0 & -3.322879 & 3.322879 \end{bmatrix},$$

$$\mathbf{J} = \begin{bmatrix} -0.125433 & 0.262725 & 0.262725 \\ 0.262725 & -0.125433 & 0.262720 \\ 0.262725 & 0.262725 & -0.125433 \end{bmatrix}.$$

And, the control parameters in (11) are chosen as $\mathrm{T}_a = 0.00049, k_a = 1810, \gamma = 200, \beta = 6000$, $\eta = 1.15, \lambda = 150, \delta = 20000$.

4.2. Coupling displacement

The pose range of the developed 3-DOF nanopositioner is from $[-80, -120, -120]^T$ to $[80, 120, 120]^T$ (unit: μm, μrad, μrad, respectively). There was a coupling displacement in $x$and $y$directions when the nanopostioner changed its pose. In some ultra-precise application scenarios, the coupling displacement should be as small as possible. The specially designed flexure diaphragm guider can reduce the coupling displacement effectively. As shown in Fig. 9, the cumulative coupling displacement are 100 nm and 120 nm in $x$and $y$directions when the nanopositioner moves from -80 μm to 80 μm in Z direction, respectively. The ratios of Z displacement to $x$and $y$coupling displacement are 1600:1 and 1333:1, respectively, which shows the nanopositioner has excellent performance in suppressing unwanted coupling displacement.

It should be mentioned that, the developed nanopositioner has a small coupling displacement within a large pose range due to the adoption of WPA and flexure diaphragm guider. Conventional stacked piezoelectric actuator usually has a travel range of tens to hundreds micrometers, however, our WPA can provide millimeter-scale travel range, so the pose range of the developed nanopositioner is able to reach from $[-80, -120, -120]^T$ to $[80, 120, 120]^T$. Moreover, the specially designed flexure diaphragm guider has a very high stiffness in $x$and $y$directions, so it can efficiently restrict the unwanted motion in these directions and thus it makes a small coupling displacement which is less than 120 nm.

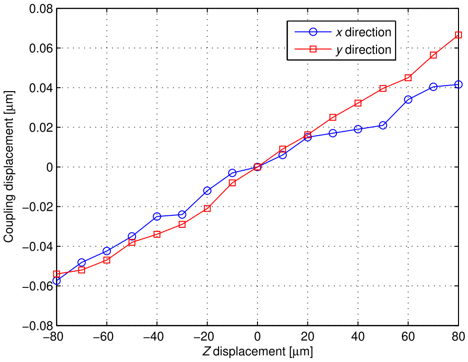

Fig. 9. The coupling displacement in $x$and $y$directions when the nanopositioner moves in Z direction.

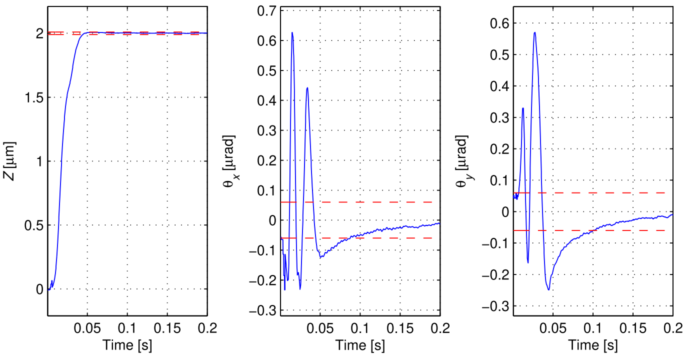

Fig. 10. The movement in Z direction.

4.3. Point-to-point movement

Typical movement in the Z direction is usually a few micrometers while there is no desired movement in the other two directions. As shown in Fig. 10, the desired pose was $[2,0,0]^T$ from the original pose $[0,0,0]^T$ and the dynamic response settled within 0.2 s. Plotted in red dashed lines, the stability error range of the pose was from $[-0.01,-0.06,-0.06]^T$ to $[0.01,0.06,0.06]^T$ centred on the desired pose. The closed-loop positioning accuracy was better than $[0.01,0.06,0.06]^T$(unit: μm, μrad, μrad, respectively).

Fig. 11 shows the movement in the θ_x direction when the desired pose was changed to $[50,10,0]^T$from $[50,0,0]^T$. Fig. 12 shows the movement in the θ_y direction when the desired pose was changed to $[-50,0,10]^T$from the pose $[-50,0,0]^T$. From the experimental results, the dynamic responses all settled within 0.2 s and the positioning accuracy was within $[0.01,0.06,0.06]^T$, clearly demonstrating the excellent movement performance of the developed nanopositioner.

It should be noted that, the developed nanopositioner has an excellent movement performance in terms of settling time and positioning accuracy due to the developed closed-loop sliding mode control strategy. The adopted motion transmission matrix can compensate for the static coupling effect between actuators and poses, which is helpful for fast dynamic response. We can see from Fig. 6c that, there is at least speed nonlinearity in WPA. The developed sliding mode control algorithm is thus adopted to overcome the effect of the nonlinearity, which can finally make the dynamic responses in all the 3-DOF Z$\theta_x\theta_y$ settling within 0.2 s and the positioning accuracy being within $[0.01,0.06,0.06]^T$.

At last, the experimental results and performance of the developed 3-DOF Z$\theta_x\theta_y$ piezoelectric driven nanopositioner are summarized in Table 2. For comparison, Table 2 also includes the performances of other similar Z$\theta_x\theta_y$ nanopositioner developed previously. It is worth mentioning that our developed nanopositioner obviously has better performance in terms of coupling displacement and nanometer scale accuracy for point-to-point movement when compared with the other two nanopositioners in this table.

5. Discussions

In the developed 3-DOF piezoelectric driven nanopositioner in this work, the adoption of WPA and flexure diaphragm guider makes the pose range being from $[-80,-120,-120]^T$ to $[80,120,120]^T$ and the coupling displacement less than

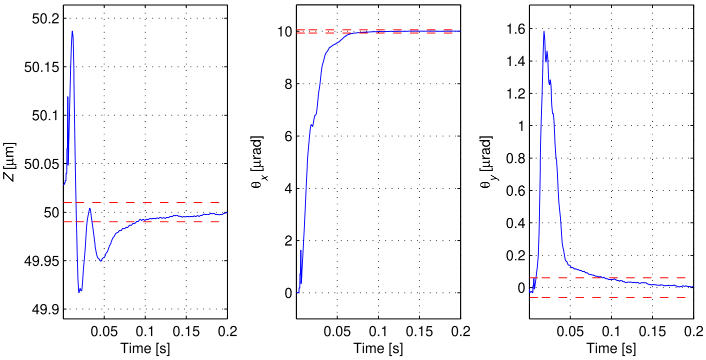

Fig. 11. The movement in θ_x direction.

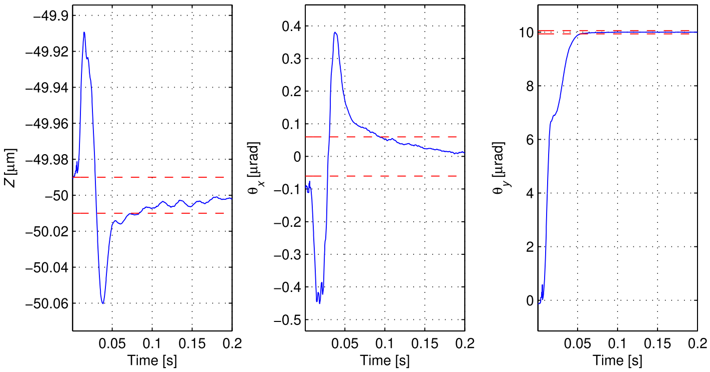

Fig. 12. The movement in θ_y direction.

Table 2
Experimental results and performance of the developed 3-DOF $Z\theta_x\theta_y$ piezoelectric driven nanopositioner (unit: µm, µrad, µrad).

	Travel range	Accuracy	Coupling displacement	Step response
This paper	160 × 240 × 240	[0.01, 0.06, 0.06]	1600:1 $(z:x)$ 1333:1 $(z:y)$	0.2 s
Ref. [16]	74.4 × −×−	[0.04, −, −]	–	0.2 s
Ref. [15]	–	[0.025, −, −]	22:1 $(z:x)$ 14:1 $(z:y)$	–

120 nm. In addition, the use of sliding mode control algorithm makes the dynamic responses in all the 3-DOF $Z\theta_x\theta_y$ settling within 0.2 s and the positioning accuracy being within $[0.01, 0.06, 0.06]^T$. With these excellent performance, the nanopositioner is especially suitable for the practical application in the objective lens as shown in Fig. 13. The objective lens is the core part of the lithography machines that are used for manufacturing integrated circuits. The objective lens consists of more than 20 individual optical lenses, some of which need nanometer scale accurate pose adjustment in order to realize ultra-precise image quality of the objective lens. During the process of the pose adjustment of individual lens, the coupling displacement in the unwanted direction should be minimized, otherwise these unwanted coupling displacement will change the position of the optical axis of the holistic objective lens and result in the deterioration of image quality. Other possible applications of the developed nanopositioner will be in biomedical devices, robotics and even on a macro-scale to structural dynamics systems.

Regarding the mechanism of the developed nanopositioner, from Fig. 2, we know that its first order resonant frequency is 173.19 Hz. One possible method of further improving the resonant frequency is to make the WPA directly drive the movable part without using the lever in Fig. 1a. In this situation, the WPA will be installed vertically inside the mechanism. However, this will also mean that, the size of the WPA needs to be smaller hence replacing the WPA for maintenance requires more time and effort.

With regard to the sliding mode control strategy, the total uncertainty of the WPA is represented by $d(t)$ in (6). One possible improvement is to further quantitatively describe the nonlinearity of the WPA such as the speed nonlinearity in Fig. 6c

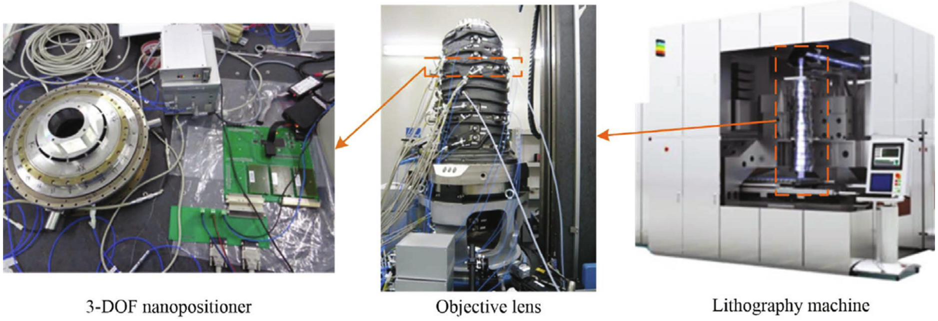
3-DOF nanopositioner Objective lens Lithography machine

Fig. 13. Application of the nanopositioner in the objective lens.

and the friction force nonlinearity. Incorporating these quantitative description of nonlinearity into the sliding mode control strategy will enable faster dynamic response and better robustness.

6. Conclusions

In this paper, a novel 3-DOF nanopositioner was investigated with a flexure diaphragm guider, capacitive sensors and walking piezoelectric actuators. The nanopositioner utilised a closed-loop sliding mode control strategy that was developed and implemented in a DSP-based micro-controller. Experimental results showed that the developed nanopositioner had excellent performance with low coupling displacement and highly accurate point-to-point movement. The ratio of coupling displacement to Z displacement was less than 0.1%. In the experiments that were undertaken, the dynamic response of point-to-point movements settled within 0.2 s and the positioning accuracy was within $[0.01\mu m, 0.06\ \mu\text{rad}, 0.06\ \mu\text{rad}]^T$. For the future work, we will investigate i) further improvement of the controller for the plant nonlinearity and uncertainty of the whole nanopositioner and ii) an application of the developed nanopositioner to position an object in the lithographic objective lens.

CRediT authorship contribution statement

Peng-Zhi Li: Conceptualization, Writing - original draft, Methodology, Data curation. **De-Fu Zhang:** Investigation, Methodology. **Barry Lennox:** Supervision, Writing - review & editing. **Farshad Arvin:** Supervision, Writing - review & editing, Funding acquisition.

Declaration of Competing Interest

The authors declare that they have no known competing financial interests or personal relationships that could have appeared to influence the work reported in this paper.

Acknowledgements

This work was supported by the UK EPSRC projects RAIN (EP/R026084/1) and RNE (EP/P01366X/1).

Appendix A

This appendix gives the proof of Lemma 1. Let $g(\psi) = |\psi| - \psi \tanh\left(\frac{\psi}{\eta}\right)$, and based on the definition of tanh function in (10), we have

$$\psi \tanh\left(\frac{\psi}{\eta}\right) = \psi \frac{e^{\frac{\psi}{\eta}} - e^{-\frac{\psi}{\eta}}}{e^{\frac{\psi}{\eta}} + e^{-\frac{\psi}{\eta}}} = \psi \frac{e^{\frac{2\psi}{\eta}} - 1}{e^{\frac{2\psi}{\eta}} + 1} = \psi\left(1 - \frac{2}{e^{\frac{2\psi}{\eta}} + 1}\right),$$

so

$$g(\psi) = \psi - \psi\left(1 - \frac{2}{e^{\frac{2\psi}{\eta}} + 1}\right) = \frac{2\psi}{e^{\frac{2\psi}{\eta}} + 1} \geqslant 0, \quad \text{if } \psi \geqslant 0,$$

and

$$\begin{aligned} g(\psi) &= -\psi - \psi\left(1 - \frac{2}{e^{\frac{2\psi}{\eta}}+1}\right) = -2\psi + \frac{2\psi}{e^{\frac{2\psi}{\eta}}+1} \\ &= -2\psi \frac{e^{\frac{2\psi}{\eta}}}{e^{\frac{2\psi}{\eta}}+1} = \frac{-2\psi}{e^{\frac{-2\psi}{\eta}}+1} > 0, \quad \text{if } \psi < 0. \end{aligned}$$

Hence, $0 \leqslant g(\psi)$ and $g(\psi)$ is an even function of ψ because $g(\psi) = g(-\psi)$.

For simplicity, we consider the scenario of the even function $g(\psi)$ when $\psi \geqslant 0$. For this scenario, we have

$$\begin{aligned}
g(\psi) &= \frac{2\psi}{e^{\frac{2\psi}{\eta}}+1},\\
\dot{g}(\psi) &= \frac{2}{\left(e^{\frac{2\psi}{\eta}}+1\right)^2}\left(1+e^{\frac{2\psi}{\eta}}-\frac{2\psi}{\eta}e^{\frac{2\psi}{\eta}}\right),\\
\ddot{g}(\psi) &= -\frac{8e^{\frac{2\psi}{\eta}}}{\eta^2\left(e^{\frac{2\psi}{\eta}}+1\right)^3}\left(\psi\left(1+e^{\frac{2\psi}{\eta}}\right)+\eta\left(1+e^{\frac{2\psi}{\eta}}-\frac{2\psi}{\eta}e^{\frac{2\psi}{\eta}}\right)\right)\\
&= -\frac{8\psi e^{\frac{2\psi}{\eta}}}{\eta^2\left(e^{\frac{2\psi}{\eta}}+1\right)^3}\left(1+e^{\frac{2\psi}{\eta}}\right)-\frac{4e^{\frac{2\psi}{\eta}}}{\eta\left(e^{\frac{2\psi}{\eta}}+1\right)}\dot{g}(\psi).
\end{aligned}$$

Based on the principles of first-derivative and second-derivative tests, when $\dot{g}(\psi)=0, \psi \geqslant 0$, then $\ddot{g}(\psi)<0$ and we have the maximum value ξ_m of the function $g(\psi)$. That is to say, when ψ satisfies

$$1+e^{\frac{2\psi}{\eta}}-\frac{2\psi}{\eta}e^{\frac{2\psi}{\eta}}=0,$$

$g(\psi)$has the maximum value ξ_m. According to the following simultaneous equations

$$\begin{aligned}
&1+e^{\frac{2\psi}{\eta}}-\frac{2\psi}{\eta}e^{\frac{2\psi}{\eta}}=0,\\
&\xi_m-\frac{2\psi}{e^{\frac{2\psi}{\eta}}+1}=0,
\end{aligned}$$

we can derive that

$$\begin{aligned}
&\frac{2\psi}{\eta}=\frac{\xi_m}{\eta}+1,\\
&\frac{\xi_m}{\eta}=e^{-\frac{2\psi}{\eta}}.
\end{aligned}$$

So, the maximum value ξ_m satisfies

$$\frac{\xi_m}{\eta}=e^{-\left(\frac{\xi_m}{\eta}+1\right)},$$

and the solution for this equation is $\xi_m/\eta=0.2785$, i.e. $\xi_m=\xi\eta, \xi=0.2785$. Thus, $|\psi|-\psi\tanh\left(\frac{\psi}{\eta}\right)\leqslant\xi\eta, \xi=0.2785$ holds.

Appendix B

This appendix gives the proof of Lemma 2. Based on $\dot{V}\leqslant-\alpha V+f$, if we define $w(t)\triangleq\dot{V}+\alpha V-f$, then we have $w(t)\leqslant 0$, and the solution of the following differential equation

$$\dot{V}=-\alpha V+f+w$$

implies that

$$V(t)=e^{-\alpha(t-t_0)}V(t_0)+\int_{t_0}^{t}e^{-\alpha(t-\tau)}f(\tau)d\tau+\int_{t_0}^{t}e^{-\alpha(t-\tau)}w(\tau)d\tau.$$

Because $w(t)\leqslant 0$ and $\forall t\geqslant t_0\geqslant 0$, we have

$$V(t)\leqslant e^{-\alpha(t-t_0)}V(t_0)+\int_{t_0}^{t}e^{-\alpha(t-\tau)}f(\tau)d\tau.$$

References

[1] Z. Sun, N. Xi, Y. Xue, Y. Cheng, L. Chen, R. Yang, B. Song, Task space motion control for AFM-based nanorobot using optimal and ultralimit archimedean spiral local scan, IEEE Robot. Autom. Lett. 5 (2) (2020) 282–289.

[2] J. Yang, C. Zhang, X. Wang, W. Wang, N. Xi, L. Liu, Development of micro- and nanorobotics: A review, Science China, Technol. Sci. 62 (1) (2019) 1–20.

[3] F. Soto, R. Chrostowski, Frontiers of medical micro/nanorobotics: Applications and commercialization perspectives toward clinical uses, Front. Bioeng, Biotechnol. 6 (2018) 170.

[4] B. Siciliano, O. Khatib, Springer handbook of robotics, Springer, 2008.

[5] S. Wang, W. Rong, L. Wang, H. Xie, L. Sun, J.K. Mills, A survey of piezoelectric actuators with long working stroke in recent years: Classifications, principles, connections and distinctions, Mech. Syst. Signal Process. 123 (2019) 591–605.

[6] G.-Y. Gu, L.-M. Zhu, C.-Y. Su, H. Ding, Motion control of piezoelectric positioning stages: modeling, controller design, and experimental evaluation, IEEE/ASME Trans. Mechatron. 18 (5) (2013) 1459–1471.

[7] P.-Z. Li, D.-F. Zhang, J.-Y. Hu, B. Lennox, F. Arvin, Hysteresis modelling and feedforward control of piezoelectric actuator based on simplified interval type-2 fuzzy system, Sensors 20 (2020) 2587.

[8] P.-Z. Li, X.-D. Wang, L. Zhao, D.-F. Zhang, K. Guo, Dynamic linear modeling, identification and precise control of a walking piezo-actuated stage, Mech. Syst. Signal Process. 128 (2019) 141–152.

[9] D.-F. Zhang, P.-Z. Li, J.-G. Zhang, H.-N. Chen, K. Guo, M.-Y. Ni, Design and assessment of a 6-DOF micro/nanopositioning system, IEEE/ASME Trans. Mechatron. 24 (5) (2019) 2097–2107.
[10] P.-Z. Li, X.-D. Wang, Y.-X. Sui, D.-F. Zhang, D.-F. Wang, L.-J. Dong, M.-Y. Ni, Piezoelectric actuated phase shifter based on external laser interferometer: design, control and experimental validation, Sensors 17 (4) (2017) 838.
[11] P.-Z. Li, P.-Y. Li, Y.-X. Sui, Adaptive fuzzy hysteresis internal model tracking control of piezoelectric actuators with nanoscale application, IEEE Trans. Fuzzy Syst. 24 (5) (2016) 1246–1254.
[12] P.-Z. Li, G.-Y. Gu, L.-J. Lai, L.-M. Zhu, Hysteresis modeling of piezoelectric actuators using the fuzzy system, The 3rd International Conference on Intelligent Robotics and Applications, vol. 6424, Springer, Shanghai, 2010, pp. 114–124.
[13] A.S. Gaunekar, G.P. Widdowson, N. Srikanth, W. Guangneng, Design and development of a high precision lens focusing mechanism using flexure bearings, Precision Eng. 29 (1) (2005) 81–85.
[14] X. Zhang, Q. Xu, Design, fabrication and testing of a novel symmetrical 3-DOF large-stroke parallel micro/nano-positioning stage, Robot. Comput. Integr. Manuf. 54 (2018) 162–172.
[15] H.S. Kim, Y.M. Cho, Design and modeling of a novel 3-DOF precision micro-stage, Mechatronics 19 (5) (2009) 598–608.
[16] K. Guo, M. Ni, H. Chen, Y. Sui, A monolithic adjusting mechanism for optical element based on modified 6-PSS parallel mechanism, Sens. Actuators: A. Phys. 251 (2016) 1–9.
[17] S. Shao, Y. Shao, S. Song, M. Xu, X. Ma, Structure and controller design of a piezo-driven orientation stage for space antenna pointing, Mech. Syst. Signal Process. 138 (2020) 106525.
[18] M. Ling, J. Cao, Z. Jiang, M. Zeng, Q. Li, Optimal design of a piezo-actuated 2-DOF millimeter-range monolithic flexure mechanism with a pseudo-static model, Mech. Syst. Signal Process. 115 (2019) 120–131.
[19] D. Sabarianand, P. Karthikeyan, T. Muthuramalingam, A review on control strategies for compensation of hysteresis and creep on piezoelectric actuators based micro systems, Mech. Syst. Signal Process. 140 (2020) 106634.
[20] A. Altan, R. Hacioglu, Model predictive control of three-axis gimbal system mounted on UAV for real-time target tracking under external disturbances, Mech. Syst. Signal Process. 138 (2020) 106548.
[21] A. Altan, R. Hacioglu, Hammerstein model performance of three axes gimbal system on unmanned aerial vehicle (UAV) for route tracking, in: 2018 26th Signal Processing and Communications Applications Conference (SIU), 2018, pp. 1–4.
[22] A. Altan, R. Hacioglu, Modeling of three-axis gimbal system on unmanned air vehicle (UAV) under external disturbances, in: 2017 25th Signal Processing and Communications Applications Conference (SIU), 2017, pp. 1–4.
[23] J. Liu, Sliding mode control using MATLAB, Academic Press, London, 2017.
[24] T.W. Seo, H.S. Kim, D.S. Kang, J. Kim, Gain-scheduled robust control of a novel 3-DOF micro parallel positioning platform via a dual stage servo system, Mechatronics 18 (9) (2008) 495–505.
[25] Y. Li, Q. Xu, A totally decoupled piezo-driven XYZ flexure parallel micropositioning stage for micro/nanomanipulation, IEEE Trans. Autom. Sci. Eng. 8 (2) (2011) 265–279.
[26] Z. Guo, Y. Tian, C. Liu, F. Wang, X. Liu, B. Shirinzadeh, D. Zhang, Design and control methodology of a 3-DOF flexure-based mechanism for micro/nano-positioning, Robot. Comput. Integr. Manuf. 32 (2015) 93–105.
[27] M. Ghafarian, B. Shirinzadeh, A. Al-Jodah, T.K. Das, Adaptive fuzzy sliding mode control for high-precision motion tracking of a multi-DOF micro/nano manipulator, IEEE Robot. Autom. Lett. 5 (3) (2020) 4313–4320.
[28] Micro-Epsilon, www.micro-epsilon.com.
[29] PiezoMotor, www.piezomotor.com.
[30] C. Edwards, S.K. Spurgeon, Sliding mode control: theory and applications, Taylor & Francis, London, 1998.
[31] M.P. Aghababa, M.E. Akbari, A chattering-free robust adaptive sliding mode controller for synchronization of two different chaotic systems with unknown uncertainties and external disturbances, Appl. Math. Comput. 218 (9) (2012) 5757–5768.
[32] M. Polycarpou, P. Ioannou, A robust adaptive nonlinear control design, Automatica 32 (3) (1996) 423–427.
[33] P.A. Ioannou, J. Sun, Robust adaptive control, Prentice-Hall, Upper Saddle River, N.J., 1995.